Sustainable Food Technology

ROYAL SOCIETY OF CHEMISTRY

PAPER

View Article Online
View Journal | View Issue



Cite this: *Sustainable Food Technol.*, 2025, **3**, 743

# The effect of nanoreinforcement geometry on the physical and structural properties of whey protein concentrate/omega-3 rich oil/$TiO_2$ nanocomposite films†

Lina María Rodríguez Pineda,‡[a] Dritan Siliqi, ‡[b] Virginia Borroni,[a] Lucas Guz,[c] Francesco Scattarella, [b] Cinzia Giannini,[b] Roberto Jorge Candal,[c] Davide Altamura*[b] and María Lidia Herrera *[a]

Whey protein concentrate (WPC)/omega-3 rich oil/$TiO_2$ nanocomposite films were prepared by casting as a bio-based alternative to petroleum-based plastics. The effect of adding Tween 20 and/or $TiO_2$ nanoreinforcement in two geometries, spheres or nanotubes (NTs), on the physical properties and structure was investigated. The initial emulsions were monomodal systems, where the maximum value of the main peak decreased with the addition of Tween 20. The addition of Tween 20 also increased the transparency of the films, while the presence of $TiO_2$ reinforcement helped block light, with nanotubes having less effect in the visible range compared to nanospheres. In comparison to the control, the Young's modulus ($E$) increased with the addition of spherical $TiO_2$ nanoparticles at a concentration of 0.2% when the formulation included Tween 20. The addition of nanotubes at 0.1% and 0.2% also enhanced the tensile and mechanical properties. The film containing 0.2% nanotubes exhibited the highest $E$, storage ($E'$), and loss ($E''$) moduli, along with the shortest elongation at break ($\varepsilon_b$) among all the films. Structural analyses using SEM, EDS, and SAXS revealed that $TiO_2$ nanospheres were prominent on the surface, particularly at the bottom of the film, while nanotubes were integrated into the bulk region of the film, forming part of the matrix. The structural description provided in this manuscript allows for the conclusion that the enhanced physical properties of nanotube-reinforced films were due to their distribution within the film matrix, which was dependent on geometry. The film reinforced with 0.2% nanotubes demonstrated potential for food packaging.

Received 27th December 2024
Accepted 10th March 2025

DOI: 10.1039/d4fb00383g

rsc.li/susfoodtech



## Sustainability spotlight

Biopolymer films have gained attention due to the harm caused by non-degradable petroleum-based plastics to marine life and the environment. Protein-based packaging is biodegradable, safer for marine life, and more eco-friendly. Finding biodegradable alternatives supports UN Goal 14 (life below water) and Goal 13 (climate action). The chosen protein, a waste product from the cheese industry, promotes circular economy principles in line with Goal 12 (responsible consumption and production). The oil used is rich in omega-3 fatty acids, supporting Goal 3 (good health and well-being). The research team, consisting of European and South American researchers with 45% women, aligns with Goals 5 (gender equality) and 17 (partnerships for the goals).

## Introduction

Films based on biopolymers have drawn much attention in the last two decades because of the marine life damage and environmental pollution caused by non-degradable plastics based on petroleum. Biopolymers, in contrast, may be degraded in the environment by microorganisms or through natural physical, chemical, and biological processes.[1] Food-grade biopolymers such as proteins, carbohydrates or lipids have been used to formulate films for packaging because they are considered safe and renewable materials.[2]

[a]*Institute of Emerging Technologies and Applied Sciences, National University of San Martín-CONICET, Campus Miguelete, 25 de Mayo y Francia, 1650 San Martín, Provincia de Buenos Aires, Argentina. E-mail: mlherrera@unsam.edu.ar*

[b]*Institute of Crystallography, National Research Council, Via Amendola 122/O, I-70126 Bari, Italy. E-mail: davide.altamura@cnr.it*

[c]*Institute of Research and Environmental Engineering, National University of San Martín-CONICET, Campus Miguelete, 25 de Mayo y Francia, 1650 San Martín, Provincia de Buenos Aires, Argentina*

† Electronic supplementary information (ESI) available. See DOI: https://doi.org/10.1039/d4fb00383g

‡ These authors (L. M. R. P. and D. S.) contributed equally.

Whey protein concentrate (WPC) is a by-product of cheese production. The whey that is a waste formed on a large scale when milk is coagulated is filtered to obtain a powder with high protein concentration. Thus, proteins are recovered for animal feed or to produce protein supplements. WPC consists of a mixture of globular proteins, including α-lactalbumin, β-lactoglobulin, serum albumin and immunoglobulins. Due to its solubility in water, gelation ability, emulsification and foaming properties, and film-forming performance, WPC was used to formulate nanocomposite films for different applications such as preservation of refrigerated meat,[3] coating sunflower seed kernels,[4] soft cheese,[5,6] and tomato packaging,[7] to name a few.

Films prepared from emulsions had the advantage of having two phases: a hydrophilic matrix and a hydrophobic discontinuous phase. The hydrophobic phase may act as a carrier for bioactive, antioxidants, or antimicrobial compounds. Different essential oils proved to be successful in delaying food spoilage and deterioration when used to formulate composite films with WPC.[4–8] Those films, with a complex two-phase matrix, effectively diffuse the essential oil within each food system, which is considered of high relevance.[8] In this way, the films containing bioactive compounds or essential oils in formulation can have active packaging characteristics.[5] In this study, we selected a commercial concentrate prepared from fish oil as a lipophilic phase because consumers appreciate omega-3 fatty acid rich food, and especially food supplemented with docosahexaenoic acid (DHA) and eicosapentaenoic acid (EPA) of marine origin. Besides, it is believed that a diet rich in DHA and EPA may have health benefits such as protection against arrhythmias and atherosclerosis.

Biopolymer-based films have poorer tensile, mechanical and barrier properties and worse UV-vis light barrier performance than plastic films which may limit the application in food packaging.[9] Addition of metal oxides to different composite films with the aim of overcoming these disadvantages has been investigated. As an approved food contact material and food additive, with quantities not exceeding 1% food weight, by the US Food and Drug Administration (FDA), $TiO_2$ nanoparticles are widely used as a polymer filler because of their easy preparation, low cost, non-toxicity, stability in the polymer matrix, antimicrobial activity against fungal and bacterial strains, and UV barrier properties.[3,10,11] The migration of $TiO_2$ nanoparticles from the composite film into the food that they are in contact with was reported to be negligible, which makes it safe for food packaging applications.[10,11] On a lab scale studying lamb meat, packed in a cellulose nanofiber/whey protein matrix containing 1% $TiO_2$ and 2% rosemary oil prepared by casting, the measured concentration coming from the packaging was very low, and well below the FDA recommended limit.[3] Migration analysis in different food simulants performed following EU standards on chitosan/$TiO_2$ nanocomposite films prepared on a laboratory scale led to the same conclusion. Migrated titanium was in a negligible amount, lower than $5.44 \times 10^{-4}$% of the total titanium in the chitosan matrix, which means that most of the titanium was retained in the polymer matrix.[12] The migration of $TiO_2$ nanoparticles was also investigated in films reinforced with spherical $TiO_2$ nanoparticles, with an average diameter of 10–40 nm, and a matrix composed of thermoplastic starch/polybutylene adipate-co terephthalate, prepared by blown-film extrusion, a method easier to scale-up.[13] According to the report, migration was mainly dependent on the hydrophilicity of the simulants, being higher for the more hydrophilic simulants. For films with $TiO_2$ concentrations between 1 and 5%, the reported total migration values ranged from 0.2 to 1.3 mg $dm^{-2}$. The amounts released were lower than those allowed by the FDA, making these films promising for food applications.[13] In this study, the selected concentrations of $TiO_2$ nanoparticles were very low, which reduces concerns regarding toxicity.

In most of the reports published in the literature, nanoreinforcements have a geometry of spheres. One of the main reasons for using $TiO_2$ P25 to improve the physical properties of biopolymer-based films is that it is commercially available. However, the reinforcement geometry is a main issue and there are only a few reports addressing the subject. Studies using whey protein nanofibrils proved that $TiO_2$ in the shape of nanotubes not only showed greater antibacterial activity than $TiO_2$ spherical nanoparticles, but also increased interactions with whey protein nanofibrils, highlighting the relevance of reinforcement geometry.[14] Our previous studies formulating films with sodium caseinate agreed with those conclusions. Data showed that nanotubes performed better as reinforcements than nanospheres regarding mechanical and tensile properties.[15] Given the literature reports, it is worth investigating the effect of nanoreinforcement geometry on films with matrices formed from globular proteins of cheese whey concentrate.

The aim of the present work was to study the effects of $TiO_2$ added in two different morphologies (spheres or tubes) on the structure and physical properties of WPC/$TiO_2$ nanocomposite films prepared from O/W emulsions formulated with concentrated-from-fish oil rich in the omega-3 fatty acids EPA and DHA.

## Materials and methods

### Starting materials

Whey protein concentrate (WPC) was purchased from Arla Food Ingredients S.A. (Buenos Aires, Argentina). It contained 80.5 ± 0.9% protein, 7.2 ± 0.6% lactose, 6.6 ± 0.3% ash, 1.8 ± 0.2% lipids, and a moisture content of 3.9 ± 0.3%. Analytical grade Tween 20, $Mg(NO_3)_2$, and glycerol were obtained from BIOPACK® (Buenos Aires, Argentina). Titanium dioxide ($TiO_2$), anatase phase with particle size < 25 nm, was purchased from Sigma-Aldrich Co. (St. Louis, MO, USA). NaOH and HCl were obtained from Merck (Nueva Jersey, EE.UU). Nutra Smart Fish Oil (Spes S.A., Santiago, Chile), a commercial food supplement rich in omega-3 fatty acids (16.600 mg/100 mL) with 14.000 mg/100 mL of EPA and DHA, was purchased in a local supermarket. For all experiments, deionized water (18 MΩ; Milli-Q Water System, Millipore Corporation, Billerica, MA, USA) was used.

### Nanotube synthesis

An alkaline hydrothermal process reported by Sayahi *et al.* (2021) and Samriti *et al.* (2022), with minor changes, was used to

 

synthesize nanotubes (NTs).[16,17] An exact weight of 420 mg of titanium dioxide was mixed with 25 g of a 10 M NaOH aqueous solution in a steel-Teflon autoclave reactor with a capacity of 50 mL. Once sealed, the device was placed in an oven at 200 °C for 24 h. After this time, consecutive washes of the product were carried out with distilled water using an ultracentrifuge (Sigma 3-18K, Sigma Laborzentrifugen GmbH, Germany) operated at 10 000 rpm (11 068 g) for 10 min per cycle, until the pH of the washing solution was less than 10. The washed solid was immersed in 100 mL of a 0.2 M HCl aqueous solution under gentle stirring for 48 h at room temperature. Subsequently, new washes were carried out to eliminate the HCl, the first three with distilled water and the following with a 1% Tween 20 aqueous solution until reaching a pH greater than 6. The NTs were kept submerged in 20.85 g of a 1% Tween 20 aqueous solution and refrigerated until use. To verify the synthesis, the morphology of the NTs was observed by scanning electron microscopy (SEM, Quanta 200, FEI, Hillsboro, TX, USA).

### Film preparation

The films were prepared from conventional oil-in-water (O/W) type emulsions. A concentration of 7.5% WPC, 6% glycerol, and 2% fish oil by weight was used. In some samples, Tween 20 was incorporated at concentrations of 0.05% or 0.1%, and $TiO_2$ nanoreinforcements in the form of spheres or nanotubes (NTs) in contents of 0.1% or 0.2% by weight, as shown in Table 1. These NT concentrations were the highest that could be added and still obtain homogeneous films when observed with the naked eye.

The first synthesis step consisted of preparing an aqueous protein solution by slowly adding an exact amount (13.4 g of 80% protein powder per 100 g) of WPC to water with constant stirring. The solution was then stirred for an additional 30 min. After the solution was prepared, the pH was adjusted to 8 using 0.5 M NaOH. The protein solution was heated at 85 °C for 20 min to denature the protein and expose its functional groups. Once the solution was cooled, water was added to maintain the mass balance of the solution.

To prepare a coarse emulsion (droplet diameter > 5 μm) in the case of the control sample, 6 g of glycerol was dissolved in 22 g of water under stirring for 5 min. Then, 70 g of the WPC solution was added to glycerol solution and stirred for 20 min. Finally, 2 g of fish oil was added (to complete a total of 100 g), and systems were homogenized using a high-speed mixer with the dispersion tool S 18N-10G (Ultra-Turrax® IKA® T18 Basic, IKA Labortechnik, Janke & Kunkel, GmbH & Co., Staufen, Germany), operated at 15 000 rpm for 1 minute. The cycle was repeated 4 times with 1 minute intervals. Samples were kept in an ice bath during processing to prevent heating.

For the samples containing $TiO_2$ in the form of nanospheres, an emulsion was prepared as in the control and the reinforcement was added in the corresponding amount after the first homogenization step with a high-speed mixer (0.1 or 0.2%). For samples with Tween 20, the content of water in glycerol solution was different than that of the control emulsion since an aqueous solution of Tween 20 was also added. In this way, the total amount of water in the formulation remained the same for all samples (Table 1). When the emulsions contained Tween 20, $TiO_2$ was added at 0.1% (5 g of 1% Tween 20 aqueous solution, the final concentration of Tween 20 in the formulation was 0.05%) or at 0.2% (10 g of 1% Tween 20 aqueous solution, final concentration of Tween 20 was 0.1%). For 0.05% Tween 20 sample, glycerol was dissolved in 17 g of water while for 0.1%, it was dissolved in 12 g. The emulsions with $TiO_2$ in spherical shape were stirred for 30 min before continuing with homogenization by ultrasound.

The control and spherical-$TiO_2$ coarse emulsions were further homogenized to obtain conventional emulsions (droplet diameters from 200 nm to 5 μm). Samples were placed in a cell with water recirculating from a bath to maintain the temperature below 20 ± 1 °C. Ultrasound was applied for 20 min using ultrasonic liquid processing equipment (Vibra Cell VC750, Sonics & Materials, Inc., Newtown, CT, USA), equipped with a 13 mm diameter and 136 mm tip length, at an amplitude of 30%.

In the case of samples with reinforcement of $TiO_2$ in NT form, after finishing ultrasound treatment, 5 g (0.1%) and 10 g (0.2%) of 1% Tween 20 aqueous solution was added. Then, emulsions were stirred for 30 min. NTs were added after the second step of homogenization because sonication breaks the NTs diminishing their length.

Finally, to obtain the films, 8 g of the emulsion were placed in polystyrene dishes with a diameter of 6 cm and dried in an oven at 30 °C for 15 h. Subsequently, the films were stored for 3 days in desiccators with a controlled atmosphere at a relative humidity (RH) of 53%, using a supersaturated solution of magnesium nitrate ($Mg(NO_3)_2$). Then, films were characterized.

Table 1 Composition of emulsions expressed in weight percentages[a] (%)

| Sample | WPC | Glycerol | Fish oil | Water | Tween 20 | Spheres | NTs |
|---|---|---|---|---|---|---|---|
| Control | 7.50 | 6.00 | 2.00 | 84.50 | — | — | — |
| Control 0.05T20 | 7.50 | 6.00 | 2.00 | 84.45 | 0.05 | — | — |
| Control 0.1T20 | 7.50 | 6.00 | 2.00 | 84.40 | 0.10 | — | — |
| 0.1$TiO_2$ | 7.50 | 6.00 | 2.00 | 84.50 | — | 0.10 | |
| 0.2$TiO_2$ | 7.50 | 6.00 | 2.00 | 84.50 | — | 0.20 | |
| 0.1$TiO_2$0.05T20 | 7.50 | 6.00 | 2.00 | 84.45 | 0.05 | 0.10 | |
| 0.2$TiO_2$0.1T20 | 7.50 | 6.00 | 2.00 | 84.40 | 0.10 | 0.20 | |
| 0.1 NT | 7.50 | 6.00 | 2.00 | 84.35 | 0.05 | — | 0.10 |
| 0.2 NT | 7.50 | 6.00 | 2.00 | 84.20 | 0.10 | — | 0.20 |

[a] T20: Tween 20; NT: nanotubes.

## Characterization of emulsions and reinforcements

### Droplet size distribution

The particle size distribution of the starting systems was determined using a laser diffraction particle size analyzer (Shimadzu SALD-3101, Shimadzu Corporation, China) with a dispersion unit model SALD-MS30 from the same manufacturer. To recirculate water, the pump was set at a flow rate of 2500 $cm^3$ $min^{-1}$. Light scattering patterns were interpreted with the Fraunhofer diffraction and Mie scattering theories. The refraction index for calculations was 1.5. To characterize the curves of number of droplets *vs.* diameter (μm), three parameters were selected: the mean diameter, the width of the distribution (difference from the 90th and 10th percentiles), and the number of particles exceeding 1 μm in diameter (% $V_{d>1}$). Determinations were conducted in triplicate and values reported are mean and standard deviations.

### $TiO_2$ nanoparticle morphology and size

$TiO_2$ nanoparticles were characterized by scanning electron microscopy (SEM) with a FEG-SEM (Supra 40, Zeiss, Oberkochen, Alemania), operated at 3 kV. Prior to imaging, a well-homogenized drop of nanoparticle solution (0.417 g of nanotubes in 20.85 g of Tween 20 solution) was diluted in distilled water (1/10 dilution), placed in a sample holder and sputter-coated with a gold layer, due to its low conductivity. The images were processed using the ImageJ software (Free software, National Institutes of Health, USA).[18] At least 300 nanoparticles from 10 images were measured and histograms were plotted for both spheres and tubes.

## Characterization of films

### Water vapor permeability (WVP)

The WVP of the films was determined following the guidelines of the ASTM E96-00 standard with slight adaptations.[15] The permeation cell employed was constructed from polyacrylate and featured a lid composed of two parallel plates. It also contains an internal compartment to place the desiccant. To maintain a relative humidity (RH) of 0% at room temperature, 20 g of dehydrated silica gel were placed within this compartment. The film, approximately 3.5 cm in diameter, was sealed between the two parallel plates positioned at the top of the cell, with rubber O-rings used to ensure a secure seal around the edges. Each plate contained a circular aperture, 2.2 cm in diameter, and was fastened in place with four screws.

The cells were placed in a desiccator containing a supersaturated aqueous solution of $Mg(NO_3)_2$ to maintain a RH of 53%. The external atmosphere of the desiccator was divided from the inside zone of the cell by the film. Water vapor passed through the film into the silica gel, increasing its mass over time. Cell mass was recorded every 24 h for 10 days. The WVP (g $h^{-1}$ $m^{-1}$ $Pa^{-1}$) was calculated using the following equation:

$$\mathrm{WVP} = \frac{\mathrm{WVT} \times e}{P_0 \times \mathrm{HR}} \quad (1)$$

where WVT is the transport of water vapor through the film, calculated as WVT = $m/A$, where $m$ is the slope of the increase in mass as a function of time (measured in grams per hour, g $h^{-1}$) and $A$ is the area of the film exposed to water vapor (measured in square meters, $m^2$); $e$ is the film thickness (measured in m); and $P_0$ is the saturation vapor pressure of water at 25 °C (3169.9 Pa).

Average values were obtained from 10 thickness measurements and used in the WVP calculations. Tests were performed in triplicate with three different films and results were expressed as mean and standard deviation.

### Water content

The humidity content was determined by weighing an exact amount of sample (~0.5 g) and drying it in an oven at 60 °C for 5 h, until constant weight is achieved. Then, humidity content was calculated as follows:

$$\mathrm{WC}(\%) = \frac{m_\mathrm{i} - m_\mathrm{f}}{m_\mathrm{i}} \times 100 \quad (2)$$

where $m_\mathrm{i}$ is the initial mass of the sample and $m_\mathrm{f}$ is the mass at the end of the assay. Experiments were done in triplicate with three different films, and results were expressed as mean and standard deviation.

### Water solubility

Solubility was determined using the methodology reported by Yu *et al.* (2023) with minor changes.[19] Films were dried at 60 °C until a constant weight was achieved. Samples were placed in beakers with 50 mL of bidistilled water and were kept at ambient temperature for 24 h. The remains of the films (not dissolved under these conditions) were dried at 60 °C for 16 h and the weight was determined. Solubility in percentage was calculated as follows:

$$\mathrm{WS}(\%) = \frac{m_1 - m_2}{m_1} \times 100 \quad (3)$$

where $m_1$ is the initial mass of the dried sample and $m_2$ is the mass of the dried remaining film at the end of the assay.

### Colour measurement

CIELab coordinates ($L^*$, $a^*$ $y$ $b^*$) were measured using a colour portable reader (CR-20, Konica Minolta, Ramsey, USA) on the top surface of films. The light source was a xenon lamp. For white calibration, a standard illuminant (D65) was selected, performing measurements with an observation angle of 10°, in a random way, on 10 points of the top surface. For each formulation, experiments were run in triplicate evaluating three different specimens. Results were average and mean values were used to calculate colour difference ($\Delta E$), which is defined as the numerical distance between two colours within the CIELab space and is calculated using the following equation:

$$\Delta E = ((\Delta L^*)^2 + (\Delta a^*)^2 + (\Delta b^*)^2)^{1/2} \quad (4)$$

### Opacity

Data were collected in a spectrophotometer (Shimadzu UV – 2401PC, Shimadzu Corporation, China). Films were cut into 2 cm × 5 cm rectangles for analysis. Absorbance was measured at 600 nm through an optical path ($b$) of 1 cm wide and 3 cm height. The thickness of the film was measured with a manual digital micrometer (Asimeto, Hong Kong, China). Opacity of the films was calculated according to Zhang and Rhim (2022) with the following equation:[10]

$$A = \frac{\text{Abs } 600 \text{ nm}}{b(\text{mm})}$$

where $A$ is the opacity and $b$ is the thickness of the film. Two films were evaluated in triplicate and results were expressed as mean and standard deviation.

### UV-visible light transmission

The light transmittance of the films was measured with an UV-vis spectrophotometer (Shimadzu UV – 2401PC, Shimadzu Corporation, China) in the range of 200 to 800 nm using air as a reference.[20] The film sample was cut into 50 mm × 30 mm strips and then placed on a sample grid. Three measurements on three different films were done and the results were expressed as the mean value and standard deviation.

### Tensile properties

Uniaxial tensile parameters were evaluated with a dynamometer (Instron 5982, Instron, Norwood, USA). The Young's modulus ($E$), tensile strength ($\sigma_b$), and elongation at break ($\varepsilon_b$), were calculated from stress–strain curves. Tests were performed at a crosshead speed of 10 mm $min^{-1}$ and a temperature of 25.00 ± 0.01 °C. The selected method was the standard test method for tensile properties of plastics using microtensile specimens (ASTM D1708). For the tests, specimens in the shape of the letter H were cut from the films with a metal template. Dimensions were 3.8 cm wide, 1.5 cm high and a central bar 0.5 cm high and 2.2 cm wide. Ten samples obtained from at least three different films were analysed. Results were reported as mean and standard deviation.

### Dynamic mechanical analysis

Storage ($E'$) and loss ($E''$) moduli were measured with a dynamic mechanical analysis machine (DMA) using a DMA 8000 (PerkinElmer, Chicago, USA) with controlled temperature and RH chamber. The temperature was set at 25 °C. A RH of 53% was selected. The experiments were performed in tension mode and within the linear viscoelastic range. Experiments were run applying a strain of 0.05%. Modulus values were obtained from a frequency scan of 1 to 10 Hz. The films were placed in the cell and samples were held using tensile test clamps. Rectangular samples with 40 mm length and 8 mm width were cut. The width was measured with a calliper and the thickness with a manual digital micrometre (Asimetro, Hong Kong, China). Assay results are reported as the average of ten samples coming from at least three different films.

### Fourier transform infrared spectroscopy

The functional groups of films were analysed by Fourier Transform Infrared Spectroscopy (FTIR) using an IR spectrometer (IR Affinity-1, Shimadzu, Tokyo, Japan), performing 40 scans with a resolution of 4 $cm^{-1}$. Background was corrected to eliminate the interference of humidity and $CO_2$ using the software provided with the equipment (IR Solutions, v. 1.5). Data were drawn and evaluated using the software OriginPro (8.5.0 V90E, Origin Lab Corporation, Northampton, MA, USA). Spectra were recorded in duplicate analysing two different films.

## Microstructural analysis

### Scanning electron microscopy (SEM)

Films were cut in rectangles of 2 × 2 mm. Both, top and bottom faces were placed on carbon tape. Then, samples were metallized using gold and were observed with an environmental scanning electron microscope (ESEM), (FEI ESEM, Quanta 200, FEI, Hillsboro, TX, USA). Images were taken with a magnification of 2500×. SEM images were analysed using Texture image analysis by using the Gray Level Co-Occurrence Matrix (GLCM) and FracLac plugin of ImageJ v 1.54k (National Institutes Health, Bethesda, MD, USA).[18] Images were converted from RBG colour to grayscale to be analysed. The selected parameters were Energy, Contrast, Homogeneity, Entropy, Lacunarity and Fractal dimension. Regarding nanoreinforcement distribution in films, the compositional mapping performed on the top and bottom faces of samples containing $TiO_2$ was done using energy dispersive spectroscopy (EDS) with an EDS (Oxford SDD X-Act, Oxford Instruments NanoAnalysis, Bucks, UK) operated under $2 \times 10^{-5}$ Pa vacuum and with an electron beam acceleration of 20 keV. Data were acquired with the AZTecOne system.

### Small angle X-ray scattering (SAXS)

SAXS measurements were performed in a laboratory SAXS instrument, (Xeuss 2.0, Xenocs, France). The X-ray wavelength for all runs was 1.542 Å (Cu source). SAXS and WAXS were measured simultaneously. For WAXS studies, a 100 K Dectris Pilatus 2D detector was used while for SAXS analysis a 200 K Dectris Pilatus 2D detector was employed. Sample to detector distances were 158.33 mm and 3790.09 mm for WAXS and SAXS, respectively. With $q = (4\pi/\lambda)\sin(\theta) = 2\pi/d$ being the scattering vector modulus, $2\theta$ the scattering angle, and $d$ the $d$-spacing, the scattering intensity was collected in the $q$-range 0.0026 to 0.1105 $Å^{-1}$, for SAXS experiments, and in the $q$-range 0.8574 to 2.5812 $Å^{-1}$, for WAXS experiments. The SAXS patterns were recorded with exposure times of 100 seconds and a resting time of 1 min. Samples were scanned horizontally in 16 consecutive spots with the last four spots located outside the sample, for 16 vertical lines. A total area of 16 $mm^2$ per sample was scanned, with a lateral step size of 0.25 mm, including a 4 $mm^2$ empty region for data normalization and monitoring of primary beam fluctuations. The transmitted X-ray intensity was obtained at the end of the SAXS and WAXS measurements during 1 s per spot in the same area. For each

sample, the 2D SAXS and WAXS patterns and the X-ray transmitted (unscattered) beam intensity were obtained. The images were generated by using the SUNBIM software, available at http://www.ba.ic.cnr.it/softwareic/sunbimweb/.[21] Normalization of the scattering data to the transmission coefficient ($T$), and calculation of the relative density/thickness distribution ($\log T$) were carried out by using the SUNBIM tools as discussed in Scattarella *et al.*, 2021.[22]

## Statistical analysis

One-way ANOVA analysis was used to determine significant differences among samples. Pairs of mean values were compared with Tukey's test. The selected $\alpha$ was 0.05.

## Results and discussion

### Droplet size distribution of the initial systems

Fig. 1 shows the particle size distribution for the control sample and the control with addition of two amounts (0.05 and 0.1%) of Tween 20. As may be observed, all distributions were almost monomodal, presenting a main population that represented a percentage greater than 90% of the total. The maximum value of the main peak shifted to the left for addition of Tween 20. The calculated parameters of the distribution are reported in Table 2. The % $V_{d>1\mu m}$ significantly decreased when Tween 20 was present in the formulation, indicating the strong interactions among protein molecules and Tween 20. A similar effect was reported when disaccharides such as trehalose or sucrose were present in sodium caseinate-stabilized emulsion formulations. The presence of small molecules with a free $OH^-$ modified protein functionality at the interface and led to a decrease in droplets size. These molecules may work as coadjuvants helping the protein to coat oil droplets or may change the quality of water as a solvent enhancing protein performance as an emulsifier.

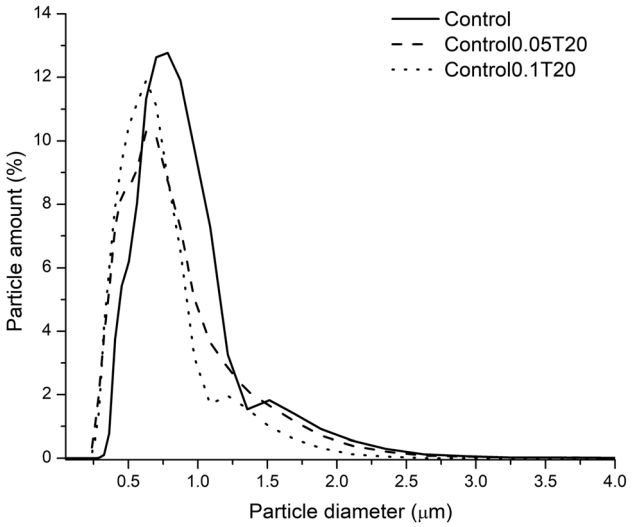


Fig. 1 Particle size distribution for the control emulsion and control with Tween 20 (T20) at 0.05 and 0.1%.

Table 2 Distribution parameters calculated from the particle amount *vs.* diameter curves

| Sample | Mean diameter (μm) | % $V_{d>1\mu m}$ (%) | Width (μm) |
|---|---|---|---|
| Control | 0.719 ± 0.019[a] | 17.333 | 0.637 |
| Control 0.05T20 | 0.579 ± 0.005[b] | 12.937 | 0.726 |
| Control 0.1T20 | 0.562 ± 0.009[b] | 7.314 | 0.511 |

### Nanotube characterization

Fig. 2 shows the SEM images of $TiO_2$ nanoparticles. The image on the left corresponds to spheres (a) and the one on the right to tubes (b). The morphologies found in Fig. 2a and b proved that tube synthesis was successful. Fig. 2 also reports the histograms of the sphere diameter (c), the tube diameter (d) and the tube length (e). Statistical analyses are shown in the ESI (Tables S1–S3).† As shown in Fig. 2c, for reinforcement in spherical shape, the histogram corroborated manufacture specifications. The mean value of particles was 22.08 ± 5.07 nm.

In the case of tube diameter (Fig. 2d), the most frequent diameter was 0.14 μm, and the mean diameter was 0.18 ± 0.09 μm. Around 83% of the diameter values were below 0.30 μm, showing a fair homogeneity of the nanotubes in this dimension.

Data reported in Fig. 2e showed that most of the nanotubes had a length between 2.26 and 25.84 μm, with a mean of 12.34 ± 4.50 μm, and a mode of 10.28 μm. Although tubes are nano in one dimension, the length in the microns excluded them from toxicity concerns.

### Film characterization

**Water vapor permeability (WVP), water content (WC), and water solubility (WS).** Table 3 summarizes thickness and WVP among other film properties. Addition of reinforcement in the low concentrations selected in this study did not significantly modify solid content and, therefore, as expected, differences among film thickness were within the experimental error. Thus, the differences found in WVP were most likely due to differences in film structure. When Tween 20 was added to the control sample at the lowest concentration (0.05%), WVP slightly increased. This result showed that Tween 20 strongly interacted with protein, which was expected, given that Tween 20 is a surfactant. The fact that the value increased indicated negative interactions most likely because the matrix structure was disrupted as observed in other systems.[15]

As the content was not high enough, changes did not occur on the whole matrix, and therefore, the barrier to water vapor was less efficient than the one of the control film. At the higher concentration used (0.1%), however, the distribution was more homogeneous and there were no significant differences in WVP values with the control film. The same behaviour was found for the film with $TiO_2$ in spheres that did not contain Tween 20. At the lower concentration the reinforcement weakened the water barrier while at the highest concentration there were no

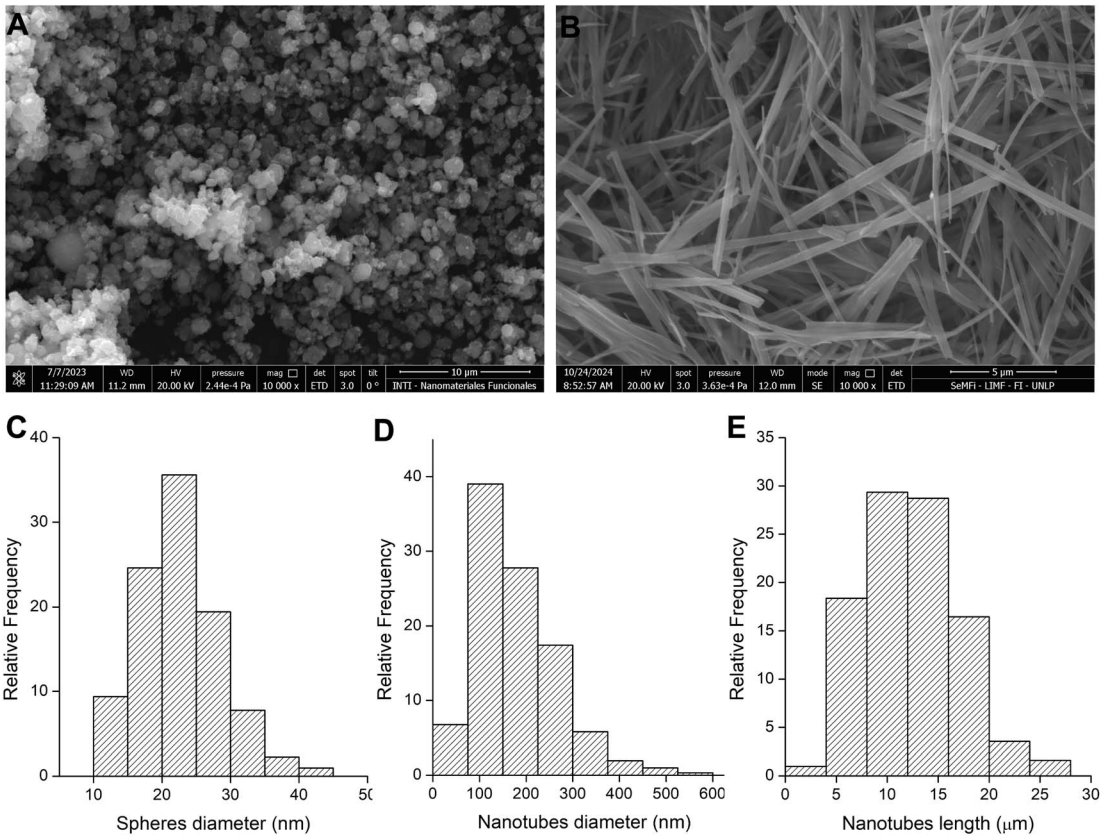


Fig. 2 SEM images of $TiO_2$ nanoparticles, (A) spheres, (B) tubes, and histograms of sphere diameter (C), of the tube diameter (D) and of the tube length (E).

Table 3 Water vapor permeability (WVP), film thickness ($t$), water content and water solubility for all films[a]

| Film | $t$ (mm) | WVP (g Pa$^{-1}$ h$^{-1}$ m$^{-1}$) × 10$^7$ | WC (%) | WS (%) |
|---|---|---|---|---|
| Control | 0.41 ± 0.04$^{a}$ | 8.96 ± 0.35$^{a,b,c}$ | 11.76 ± 1.25$^{a}$ | 48.57 ± 1.92$^{a}$ |
| Control 0.05T20 | 0.44 ± 0.03$^{a}$ | 10.56 ± 0.71$^{d,e}$ | 11.26 ± 1.49$^{a}$ | 48.93 ± 2.31$^{a}$ |
| Control 0.1T20 | 0.45 ± 0.06$^{a}$ | 9.67 ± 0.53$^{c,d}$ | 11.09 ± 0.95$^{a}$ | 50.29 ± 3.00$^{a}$ |
| 0.1$TiO_2$ | 0.43 ± 0.03$^{a}$ | 10.82 ± 0.45$^{d,e}$ | 11.26 ± 1.49$^{a}$ | 47.35 ± 3.77$^{a}$ |
| 0.2$TiO_2$ | 0.43 ± 0.07$^{a}$ | 7.69 ± 0.08$^{a,b}$ | 10.93 ± 1.61$^{a}$ | 47.72 ± 1.55$^{a}$ |
| 0.1$TiO_2$0.05T20 | 0.40 ± 0.09$^{a}$ | 7.40 ± 0.26$^{a}$ | 10.89 ± 1.28$^{a}$ | 48.10 ± 3.22$^{a}$ |
| 0.2$TiO_2$0.1T20 | 0.50 ± 0.02$^{a}$ | 8.91 ± 0.19$^{b,c}$ | 11.13 ± 1.20$^{a}$ | 47.72 ± 1.55$^{a}$ |
| 0.1 NT | 0.40 ± 0.04$^{a}$ | 10.09 ± 0.79$^{c,d}$ | 11.32 ± 1.22$^{a}$ | 48.10 ± 3.22$^{a}$ |
| 0.2 NT | 0.43 ± 0.05$^{a}$ | 11.81 ± 0.78$^{e}$ | 11.38 ± 0.74$^{a}$ | 47.53 ± 1.69$^{a}$ |

[a] T20: Tween 20; WC: water content; WS: water solubility; data in the same column with the same capital letter are not significantly different ($p < 0.05$).

significant differences with the control film. For spherical reinforcement, WVP values improved when the film also contained Tween 20. The film with 0.2% NTs had the highest WVP value of all films prepared, showing significant differences with the control, suggesting a different organization of the building blocks of the matrix. However, WVP values for all samples were close and in the order of the ones reported in the literature for other systems.[11]

Water content and solubility showed no significant differences among samples ($p < 0.05$), indicating that these properties were not significantly affected by the presence of Tween 20 and nanoreinforcements at the selected concentrations (Table 3). $TiO_2$ and Tween 20 were used in very low amounts that did not change the hydrophilicity of the films. The average water content considering all formulations was 11.22%, which was half the content reported for starch films and the average solubility was 48.26%, which was twice the solubility reported for those starch nanocomposites.[20] However, similar values were found for systems with a protein/carbohydrate matrix such as sodium caseinate/guar gum/$TiO_2$/cumin essential oil composite film.[23]

Table 4 CIElab coordinates ($L^*$, $a^*$, $b^*$), total color change ($\Delta E$) for different effects, and opacity for all films

| | Color (CIELab) | | | $\Delta E$ | | | |
|---|---|---|---|---|---|---|---|
| Film | $L^*$ | $a^*$ | $b^*$ | T20 | $TiO_2$ | Geometry | Opacity ($mm^{-1}$) |
| Control | $78.45 \pm 1.40^a$ | $0.50 \pm 0.15^a$ | $16.75 \pm 1.09^a$ | | | | $2.19 \pm 0.17^a$ |
| Control 0.05T20 | $78.00 \pm 2.21^a$ | $0.42 \pm 0.19^a$ | $18.52 \pm 2.37^a$ | 1.83 | | | $1.64 \pm 0.08^a$ |
| Control 0.1T20 | $78.39 \pm 2.28^a$ | $0.38 \pm 0.28^a$ | $18.37 \pm 2.83^a$ | 1.62 | | | $1.92 \pm 0.29^a$ |
| $0.1TiO_2$ | $81.11 \pm 0.93^a$ | $2.04 \pm 0.40^b$ | $27.17 \pm 0.69^b$ | | 10.86 | | $5.30 \pm 0.15^b$ |
| $0.2TiO_2$ | $82.34 \pm 1.60^a$ | $2.33 \pm 0.76^b$ | $25.32 \pm 1.71^b$ | | 9.58 | | $6.36 \pm 0.08^c$ |
| $0.1TiO_20.05T20$ | $81.02 \pm 1.46^a$ | $1.78 \pm 0.84^b$ | $26.18 \pm 3.72^b$ | | 8.34 | | $7.31 \pm 0.15^d$ |
| $0.2TiO_20.1T20$ | $81.64 \pm 0.66^a$ | $1.99 \pm 0.66^b$ | $26.39 \pm 2.55^b$ | | 8.81 | | $5.36 \pm 0.09^b$ |
| 0.1 NT | $79.06 \pm 3.40^a$ | $1.28 \pm 0.71^a$ | $25.02 \pm 4.88^b$ | | 6.64 | 2.32 | $4.73 \pm 0.55^b$ |
| 0.2 NT | $83.54 \pm 0.75^b$ | $0.85 \pm 0.56^a$ | $23.58 \pm 2.07^b$ | | 7.35 | 3.55 | $5.31 \pm 0.31^b$ |

**Colour and opacity of films.** Table 4 summarizes CIELab coordinates, total colour changes and opacity for all films. Addition of Tween 20 did not modify parameter $L^*$. In contrast, compared to the control film, addition of nanotubes of $TiO_2$ in an amount of 0.2% significantly increased parameter $L^*$. These films were whiter than the control. Formulations with Tween 20 had the same redness (parameter $a$) than the control film. For films with spherical nanoparticles of $TiO_2$ ($0.1TiO_2$, $0.2TiO_2$, $0.1TiO_20.05T20$, and $0.2TiO_20.1T20$), parameter $a^*$ significantly increased. However, when the reinforcement had nanotube geometry, parameter $a^*$ remained unchanged, indicating the relevance of geometry on the colour of films. The parameter $b^*$ significantly increased upon the addition of $TiO_2$. The films were yellower than the control for both $TiO_2$ concentrations and both reinforcement geometries, spheres or tubes. Tween 20 had no effect on parameter $b^*$. In agreement with the parameter's changes, total colour change due to Tween 20 was low. $TiO_2$ films showed significant total colour changes compared to their corresponding controls, being higher for spherical $TiO_2$ reinforcement films. Opacity of films was not modified by the addition of Tween 20. On the other hand, $TiO_2$ reinforcement significantly increased opacity, being higher for spheres than nanotubes. Selecting a geometry of nanotubes for the reinforcement could be an advantage since in some food applications less colour and opacity could be desirable. However, values of opacity were suitable in all cases and lower than the ones reported for other systems in the literature. For films based on sodium caseinate solution, opacity values ranged from 7.26 to 18.00 $mm^{-1}$, whereas for whey protein isolate-based films plasticised with varying concentrations of *Apis mellifera* honey, the opacity values ranged from 14.51 to 16.02 $mm^{-1}$.[15,24]

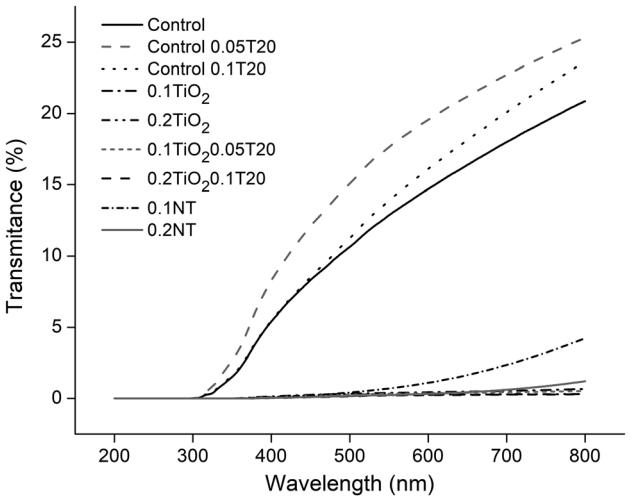


Fig. 3 UV-vis transmittance spectra of all films.

### UV- visible light transmission

Fig. 3 reports the UV-vis transmittance spectra of all films. The control films transmitted light above 300 nm, with the films containing Tween 20 exhibiting the greatest transparency. Films incorporating spherical particles of $TiO_2$ were highly effective in blocking light in the range of 200 to 800 nm, with transmitted light remaining below 1%. Consistent with the significant changes observed in colour and opacity compared to the control films, the films containing spherical particles of $TiO_2$ also altered the ability to block light, demonstrating excellent blocking efficiency across the 200 to 800 nm range. While films containing nanotubes were also effective in blocking UV light, some transmission occurred in the 500–800 nm range, particularly when the nanotube concentration was 0.1%. From the results reported in Fig. 3, it may be noticed that Tween 20 increased the transparency of films while $TiO_2$ reinforcement helped block light, with nanotubes having less effect in the visible zone than nanospheres.

### Tensile and mechanical properties

Table 5 summarizes the tensile and mechanical properties of all films calculated from the experimental data shown in Fig. S1 and S2.† Compared to the control, the Young's modulus $E$ increased by addition of spherical $TiO_2$ nanoparticles at 0.2% concentration when the formulation had Tween 20 ($0.2TiO_20.1T20$). It is likely that Tween 20 enhanced interactions among protein molecules leading to a more elastic structure. The films with nanotubes at the two concentrations selected in this study also had higher $E$ than the control, with the film containing 0.2% nanotubes having the highest $E$ modulus and the shorter elongation at break ($\varepsilon_b$) of all films. The highest effect of nanotubes showed the relevance of reinforcement

 

Table 5 Tensile and mechanical properties for all films[a]

| Film | $E$ (MPa) | $\sigma_b$ (MPa) | $\varepsilon_b$ (%) | $E'$ (Mpa) | $E''$ (Mpa) |
|---|---|---|---|---|---|
| Control | $7.25 \pm 0.92^{a}$ | $0.66 \pm 0.08^{a,d}$ | $67.61 \pm 15.40^{a,b}$ | $9.46 \pm 1.34^{a}$ | $2.58 \pm 0.43^{a}$ |
| Control 0.05T20 | $5.86 \pm 0.91^{b}$ | $0.54 \pm 0.06^{b}$ | $63.95 \pm 15.27^{a,b}$ | $9.70 \pm 1.27^{a}$ | $2.46 \pm 0.32^{a}$ |
| Control 0.1T20 | $6.34 \pm 0.75^{a,b}$ | $0.58 \pm 0.06^{a,b,c}$ | $68.87 \pm 15.23^{a,b}$ | $9.72 \pm 1.20^{a}$ | $2.57 \pm 0.19^{a}$ |
| $0.1TiO_2$ | $6.44 \pm 0.66^{a,b}$ | $0.63 \pm 0.04^{a,c,d}$ | $73.26 \pm 11.40^{a}$ | $9.21 \pm 1.58^{a}$ | $2.45 \pm 0.48^{a}$ |
| $0.2TiO_2$ | $6.57 \pm 0.36^{a,b}$ | $0.61 \pm 0.07^{a,b,c}$ | $66.66 \pm 15.37^{a,b}$ | $10.20 \pm 1.30^{a}$ | $2.77 \pm 0.42^{a}$ |
| $0.1TiO_20.05T20$ | $6.44 \pm 0.37^{a,b}$ | $0.56 \pm 0.08^{b,c}$ | $60.56 \pm 15.55^{a,b,c}$ | $10.45 \pm 1.54^{a,b}$ | $2.90 \pm 0.41^{a,b}$ |
| $0.2TiO_20.1T20$ | $8.31 \pm 0.77^{c}$ | $0.71 \pm 0.09^{d}$ | $68.08 \pm 14.23^{a,b}$ | $10.36 \pm 1.56^{a}$ | $2.89 \pm 0.26^{a}$ |
| 0.1 NT | $9.98 \pm 0.92^{d}$ | $0.71 \pm 0.08^{d}$ | $55.58 \pm 13.59^{c}$ | $12.52 \pm 2.28^{b,c}$ | $3.48 \pm 0.63^{b,c}$ |
| 0.2 NT | $11.70 \pm 0.79^{e}$ | $0.72 \pm 0.10^{d}$ | $45.74 \pm 8.80^{c}$ | $13.79 \pm 1.29^{c}$ | $3.85 \pm 0.45^{c}$ |

[a] Young's modulus: $E$; the ultimate strength: $\sigma_b$; elongation at break: $\varepsilon_b$; storage modulus: $E'$, and loss modulus: $E''$. $E'$ and $E''$ were measured at 1 Hz.

geometry. These films also contained Tween 20 that strongly interacted with the building blocks of the protein structure. Films reinforced with nanotubes also showed better mechanical properties than the other films, with $E'$ and $E''$ being significantly higher than those of the control. Addition of nanotubes improved the tensile and mechanical properties of films at the low concentrations used, with $E$ and $E'$ values being close to the ones reported for protein-based films with spherical reinforcements at higher concentrations.[11]

### FTIR analysis

Fig. 4 reports FTIR spectra expressed as absorbance *vs.* wavenumbers for all films. Signal assignments were done considering data reported in the literature.[1,25] In all spectra, the signal at 3291 $cm^{-1}$, attributed to amide A in the literature, was broad. This band is typical of proteins and corresponds to N–H stretching. The signal that appeared at 2926 $cm^{-1}$ was also due to N–H stretching and was assigned to amide B. The signal at 2850 $cm^{-1}$ was due to CH–$CH_2$ stretching of carbon chains of oil. The maximum absorbance of the three signals and their positions showed no significant differences among samples.

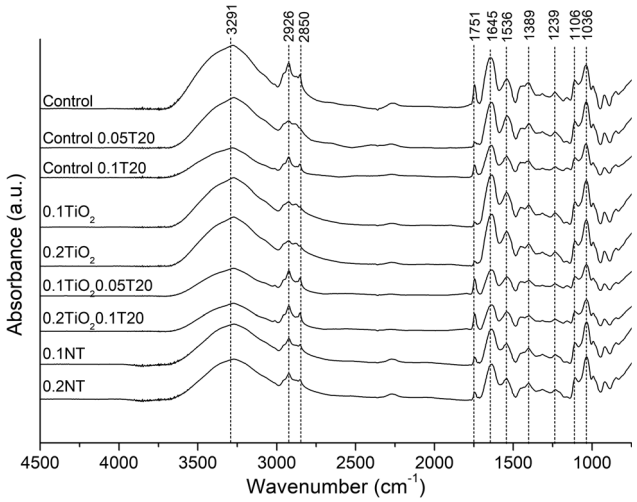


Fig. 4 Fourier Transformed Infrared (FTIR) spectra expressed as absorbance *vs.* wavenumbers for all samples obtained using attenuated total reflectance mode.

The signal at 1751 $cm^{-1}$ was assigned to the C=O groups of oil. The signal was less intense for films with Tween 20 and nanoreinforcements, especially for nanotubes, indicating that oil was more encapsulated in the film matrix when Tween 20 was added and when the films were reinforced. The signal at 1645 $cm^{-1}$, corresponding to amide I (C=O group), also diminished when Tween 20 and reinforcements were added, indicating strong interactions among components. The lower intensity of the band may also indicate the formation of covalent bonds between Tween 20 $OH^-$ and C=O groups.

However, if the reaction occurred, it did not take place on a large scale, considering the changes in signal intensity. The signals at 1536, 1389, and 1239 $cm^{-1}$ were attributed to N–H (amide II), $COO^-$, and C–N (amide III) stretching, respectively. There were no significant differences in position and intensity for these bands among samples. The signals that appeared at 1106 and 1036 $cm^{-1}$ are characteristic of primary and secondary alcohols and correspond to C–O stretching in C–OH bonds.[26,27] These signals did not change significantly, reinforcing the hypothesis that crosslinking between protein and Tween 20 did not occur to a great extent in WPC-based films as was reported for sodium caseinate.[15] WPC proteins have a globular nature with a spherical structure induced by their tertiary structure. For this reason, in WPC proteins the functional groups are less exposed than in disordered proteins such as sodium caseinate and showed less tendency to form ester functions with Tween 20 than sodium caseinate.

### Film structure and nanoreinforcement distribution by SEM

Fig. 5 reports SEM images of the upper and lower surfaces of films containing Tween 20, reinforced with 0.2% $TiO_2$ nanospheres ($0.2TiO_20.05T20$) or 0.2% $TiO_2$ nanotubes (0.2 NT). The control samples, consisting of films reinforced with spheres but without Tween 20, and those containing Tween 20 along with 0.1% nanoreinforcement in either spherical or tubular forms, are shown in Fig. S3–S5,† respectively. The control films exhibited smooth surfaces devoid of cracks or protruding features (Fig. S3†). Images in Fig. 5, S4, and S5† showed that, in comparison to the control, the reinforced films displayed significant structural differences. The surfaces exhibited distinct characteristics resulting from the interactions between the matrix and the reinforcement. $TiO_2$ nanospheres were

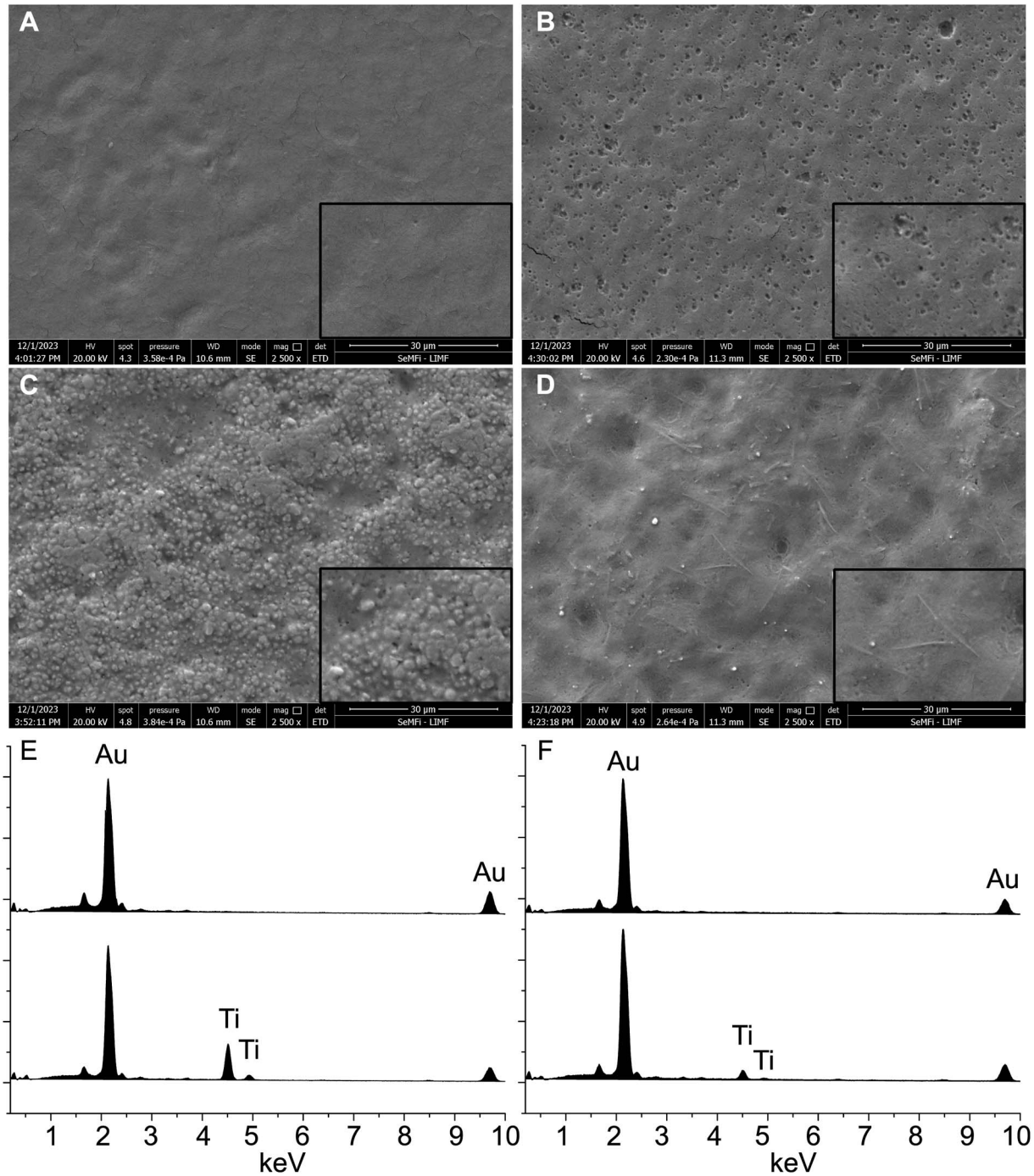


Fig. 5 SEM micrographs of the upper surface (A and B) and lower surface (C and D) of films reinforced with nanospheres (A and C) or nanotubes (B and D). Scale bar 30 μm. Inset 10 μm. EDS signals from films reinforced with nanospheres (E) or nanotubes (F). Upper trace corresponds to the upper surface and lower trace to the lower surface. Scale bar 30 μm.

prominent on the surface, particularly at the bottom of the film. The images revealed spherical objects covering the entire surface (Fig. 5a and c). Conversely, nanotubes were integrated into the bulk region of the film, forming part of the matrix (Fig. 5b and d). Fig. 5e and f present the results of evaluating the distribution of $TiO_2$ nanoparticles on the upper and lower surfaces using EDS. The distributions indicated that the upper surfaces of both the nanosphere (Fig. 5e) and NT (Fig. 5f) reinforced films contained no $TiO_2$, suggesting that most of the reinforcement was situated on the bottom surface or in bulk. The intensity of the signals from the bottom surface of $TiO_2$ nanotube films (Fig. 5f) was significantly lower than that of the $TiO_2$ nanospheres (Fig. 5e), indicating that there was a different distribution of reinforcement depending on geometry. Fig. S6a–c† show cryofracture images for nanotube-reinforced films revealing the complete thickness of the film. It is evident from

 

the images that the reinforcement is located within the inner part of the film, interconnecting the building blocks of the matrix (Fig. S6c†). The differences in signal intensities measured on the bottom surface, as shown in Fig. 5e and f, and the cryofracture images reported in Fig. S6† confirmed that nanotubes were incorporated within the thickness of the films, reinforcing the bulk zone of the matrix, whereas the spheres were located on the bottom surface. This structural difference between nanospheres and NT-reinforced films led to differences in mechanical and tensile properties as measured by DMA and tensile tests.

Table 6 reports the texture parameters of films calculated from images shown in Fig. 5 and S3–S5.† The texture of an image is defined as the local variation in brightness between one pixel and another, arranged in different greyscales or within a small area. Image texture has been utilised for pattern identification to characterise the arrangement of the basic constituents of a material's surface in systems such as fried batters.[28,29]

Structure analysis parameters such as fractal dimension has been employed to measure irregularities in an image, estimate roughness, and segment textures, among other applications. This is because structural changes on the surface of a material with different formulations lead to variations in surface roughness, corresponding to different fractal dimension values.[29] Lacunarity is a parameter that complements fractal dimension in image analysis, as it measures how the data fills the space. Energy, homogeneity, contrast, and entropy are other parameters that contribute to texture image analysis. The energy parameter relates to uniformity; the higher the value, the more homogeneous the structure. The same applies to the homogeneity parameter. Conversely, higher contrast values indicate a more heterogeneous surface with more differentiated areas. Entropy is associated with the disorder of the surface; thus, the higher the entropy, the greater the heterogeneity.[30] The values obtained indicated that the Control and Control 0.05T20 samples did not show significant differences between both surfaces, suggesting that the texture was homogeneous (Table 6). However, the film containing 0.1% Tween 20 (Control 0.1T20) exhibited heterogeneity, with differences in contrast and entropy between the upper and lower surfaces. Furthermore, the upper surface of this sample was significantly different from the control in all parameters ($p < 0.01$). In other words, adding Tween 20 at the highest concentration tested (0.1%) to the control resulted in heterogeneity in the surface texture of the film.

As can be observed from Table 6, the parameters of films containing $TiO_2$ in both geometries—spheres and tubes—differ from those of the corresponding controls ($p < 0.01$). The presence of $TiO_2$ in the form of nanospheres resulted in substantial differences in the texture of the upper and lower surfaces of the films, with this effect being most pronounced in the film containing 0.2% $TiO_2$. Significant heterogeneity is observed on the lower surface where the particles are deposited, as evidenced by the highest contrast and entropy values alongside the lowest homogeneity and energy values. For films containing 0.1% $TiO_2$ and Tween 20, the differences with the corresponding control were smaller for the upper surface than for the lower surface. The inclusion of Tween 20 in the film with 0.2% $TiO_2$ enhances the homogeneity, bringing the parameters' values for the upper and lower surfaces closer.

In contrast to the effects of addition of nanospheres, the incorporation of nanotubes into the films resulted in smaller differences in texture between the upper and lower surfaces. This is particularly evident in the films with 0.2% nanotubes, which did not display significant differences in most textural parameters. In fact, these values were very similar to those of the respective control (Control 0.1T20), especially for the upper surface. The parameters of the nanotube-reinforced films

Table 6 Textural parameter calculated from SEM images for all films[a]

| Film | | Energy ($\times 10^{-4}$) | Contrast | Homogeneity ($\times 10^{-2}$) | Entropy | Lacunarity ($\times 10^{-2}$) | Fractal dimension |
|---|---|---|---|---|---|---|---|
| Control | Upper | 53.3 ± 6.5A | 21.0 ± 1.3A | 23.5 ± 0.1A | 5.6 ± 0.1A | 16.8 ± 0.2A | 1.49 ± 0.03A |
| | Lower | 54.2 ± 6.7A | 20.4 ± 0.8A | 24.0 ± 0.5A | 5.6 ± 0.1A | 14.7 ± 0.5A | 1.43 ± 0.02A |
| Control 0.05T20 | Upper | 50.4 ± 1.9A | 25.5 ± 0.5A | 21.8 ± 0.1A | 5.7 ± 0.1A | 15.7 ± 0.2A | 1.43 ± 0.02A |
| | Lower | 45.8 ± 5.1A | 23.1 ± 1.3A | 22.6 ± 0.4A | 5.8 ± 0.1A | 18.1 ± 0.2A | 1.42 ± 0.07A |
| Control 0.1T20 | Upper | 44.0 ± 8.0A | 22.8 ± 0.2A | 22.6 ± 0.1A | 5.7 ± 0.1A | 8.22 ± 0.4A | 1.56 ± 0.02A |
| | Lower | 38.5 ± 8.3A | 28.2 ± 3.8B | 21.0 ± 1.0A | 6.1 ± 0.3B | 13.3 ± 0.3B | 1.44 ± 0.03B |
| 0.1$TiO_2$ | Upper | 61.5 ± 8.9A | 16.0 ± 0.4A | 35.0 ± 0.1A | 5.4 ± 0.1A | 24.6 ± 0.9A | 1.45 ± 0.06A |
| | Lower | 15.6 ± 5.1B | 51.8 ± 5.5B | 20.0 ± 0.6B | 6.8 ± 0.1B | 8.4 ± 0.9B | 1.49 ± 0.08B |
| 0.2$TiO_2$ | Upper | 15.0 ± 5.0A | 40.8 ± 0.2A | 17.6 ± 0.1A | 6.4 ± 0.0A | 10.4 ± 0.1A | 1.52 ± 0.03A |
| | Lower | 5.8 ± 0.4B | 82.9 ± 6.8B | 12.7 ± 0.1B | 7.6 ± 0.2B | 3.22 ± 0.03B | 1.57 ± 0.03B |
| 0.1$TiO_2$0.05T20 | Upper | 6.8 ± 0.8A | 19.7 ± 1.1A | 24.2 ± 0.4A | 6.1 ± 0.1A | 11.2 ± 0.1A | 1.47 ± 0.04A |
| | Lower | 33.3 ± 4.9B | 64.0 ± 4.4B | 15.0 ± 0.2B | 7.7 ± 0.1B | 3.78 ± 0.04B | 1.51 ± 0.05B |
| 0.2$TiO_2$0.1T20 | Upper | 20.4 ± 1.1A | 41.7 ± 0.9A | 15.5 ± 0.1A | 6.7 ± 0.1A | 5.52 ± 0.01A | 1.60 ± 0.03A |
| | Lower | 7.1 ± 0.3B | 54.6 ± 3.1B | 18.2 ± 0.6B | 7.6 ± 0.1B | 2.93 ± 0.01B | 1.56 ± 0.03B |
| 0.1 NT | Upper | 17.0 ± 4.0A | 55.6 ± 2.3A | 16.7 ± 0.4A | 6.9 ± 0.2A | 8.83 ± 0.07A | 1.46 ± 0.03A |
| | Lower | 11.7 ± 4.0B | 46.8 ± 2.4B | 15.5 ± 0.3A | 7.2 ± 0.1B | 7.53 ± 0.07A | 1.45 ± 0.04A |
| 0.2 NT | Upper | 22.5 ± 4.5A | 27.8 ± 1.7A | 23.1 ± 2.5A | 6.5 ± 0.2A | 8.82 ± 0.05A | 1.52 ± 0.04A |
| | Lower | 18.2 ± 4.2A | 26.2 ± 0.9A | 21.9 ± 0.3A | 7.2 ± 0.2B | 6.98 ± 0.08A | 1.45 ± 0.04B |

[a] T20: Tween 20; across a column and in each individual sample the same capital letter indicates that the upper and lower values are not significantly different ($p < 0.01$).

exhibited significant differences compared to those of the nanosphere-reinforced films ($p < 0.01$). In the case of films containing 0.2% $TiO_2$, the differences with the corresponding control were smaller for the nanotubes than for the nanospheres, on both the upper and lower surfaces. These findings agreed with those shown in Fig. S6,† which illustrates that the nanotubes are integrated within the structure of the matrix while the nanospheres are located at the lower surface (Fig. 5e).

### Structure by X-ray analysis

Scanning X-ray microscopy with both scattering (in the small and wide-angle ranges-SAXS and WAXS, respectively) and absorption contrasts was employed to study the lateral variation of the structural/morphological properties in the films. The lateral spatial distribution is intended within the film plane (while being averaged across film thickness), thus providing complementary information to cross-SEM characterization (which on the contrary is sensitive to the distribution across film depth). SAXS microscopies were obtained by integrating and reporting on a colour scale the total SAXS intensity measured by the detector at each point on the sample. The presence of crystalline nanotubes was assessed by comparing the averaged WAXS profile from the 0.2% NT sample with the 0.2% $TiO_2$ sample (0.2$TiO_2$0.01T20, Fig. 6): weaker and slightly shifted peaks were detected from the nanotubes, although the main peak was found to be very close for nanospheres and nanotubes. To obtain higher precision, the crystalline phase of the nanospheres was verified by fitting the whole X-ray Diffraction (XRD) profile collected in $2\theta$ geometry, by using the Program EXPO (Fig. S7†).[31]

The anatase was identified as the only crystalline phase in the sample, with the derived unit cell parameters: $a = 3.78248$; $b = 3.78248$; $c = 9.50680$; $\alpha = \beta = \gamma = 90.000°$, based on the 9008213.cif file of the Crystallography Open Database (COD) [http://www.crystallography.net/].

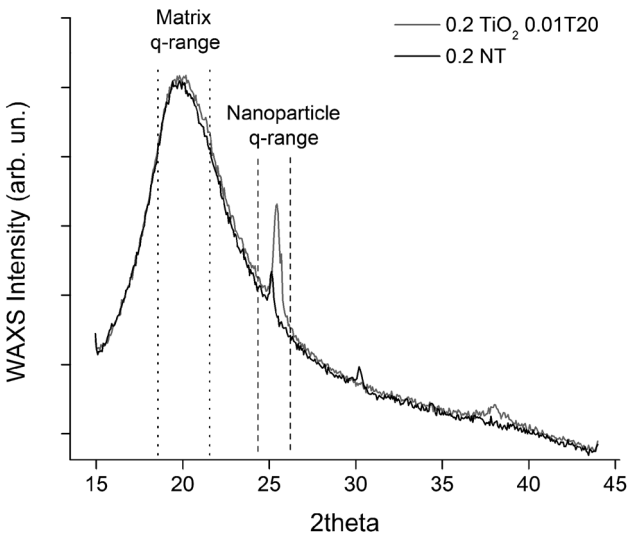


Fig. 6 Representative WAXS profiles from samples containing 0.2% nanospheres or nanotubes, averaged over the whole sample area scanned in the X-ray microscopy experiments. To plot the WAXS microscopies in Fig. 7 and S8,† the diffracted intensity was integrated in the angular ranges marked by dotted and dashed lines as mainly representative of the matrix and nanoparticle signal, respectively.

WAXS microscopies were obtained by integrating the diffracted intensity only in a given $q$-range, relevant either to the main diffraction peak of the nanoparticles (spheres or tubes) or to the wide amorphous peak of the matrix, as shown in Fig. 6. WAXS, SAXS and absorption ($n$) microscopies reported in Fig. 7 are relevant to the same samples studied in the SAXS microscopies of Fig. 8; WAXS, SAXS and absorption ($n$) microscopies reported in Fig. S8† are relevant to the same samples studied in the SAXS microscopies of Fig. S9.† More details of the histograms reported in Fig. S9† are reported in Fig. S10.† The maps obtained in the two different ranges show a similar lateral distribution of nanoparticles and matrix, proving that both components are well intermixed. Any visible gradient occurs in both components, as well as in the transmitted intensity ($I_T$) maps and in the corresponding relative density/thickness maps ($n$), indicating regions with overall density or thickness variation without segregation of either moiety. Given the full correspondence among SAXS, WAXS, and absorption microscopies, a quantitative statistical analysis based on image processing was carried out only on the SAXS and absorption microscopies, as explained in the following.

Fig. 8 presents 2D images illustrating the spatial distribution of X-ray intensity for the Control, Control with the highest Tween 20 concentration (Control 0.1T20), film reinforced with 0.2% $TiO_2$ nanospheres (0.2$TiO_2$0.1T20), and film reinforced with 0.2% $TiO_2$ nanotubes (0.2 NT). The SAXS intensity ($I_{SAXS}$) is displayed in the left column, the transmitted intensity ($I_T$) in the second column, the normalized $I_{SAXS}/I_T$ maps in the third column, and a histogram of $I_{SAXS}/I_T$ values on the right. The microscopies for the remaining films are reported in Fig. S9.† The $I_T$ maps depict the lateral variation of the X-ray absorption coefficient. $I_{SAXS}$ images were divided by the corresponding transmission coefficient maps (as in our previous articles)[22] to facilitate the observation of differences in scattering contrast independently of the local material absorption.

The distribution histograms of the $I_{SAXS}/I_T$ values obtained from the relevant images are reported in the fourth column of Fig. 8. All the histograms together are shown in Fig. S10.† The values of the statistical parameters calculated from the histograms of all films are summarised in Table S4.† It is evident that the control exhibited a very narrow distribution (range = 7040), with 88% of the data falling within the interval 225 520 to 228 000 (mode = 225 520, Table S4†). This suggests a very homogeneous distribution of the dispersing elements in the evaluated area, as depicted in the image. These results are consistent with observations from the SEM images, where the control samples exhibited smooth surfaces without pores or cracks (Fig. S3†). The addition of 0.05% Tween 20 did not alter the distribution (mode = 233 830); however, it did broaden it (range = 13 630). This indicated a strong interaction between the protein and Tween 20, which agreed with the results obtained from the FTIR analysis. When the concentration of Tween 20 is increased to 0.1%, the $I_{SAXS}/I_T$ values decrease significantly (mode = 150 870), with the highest value of the distribution (maximum = 161 170) being still lower than that in the control mode. The image exhibited a greater colour variation, reflecting

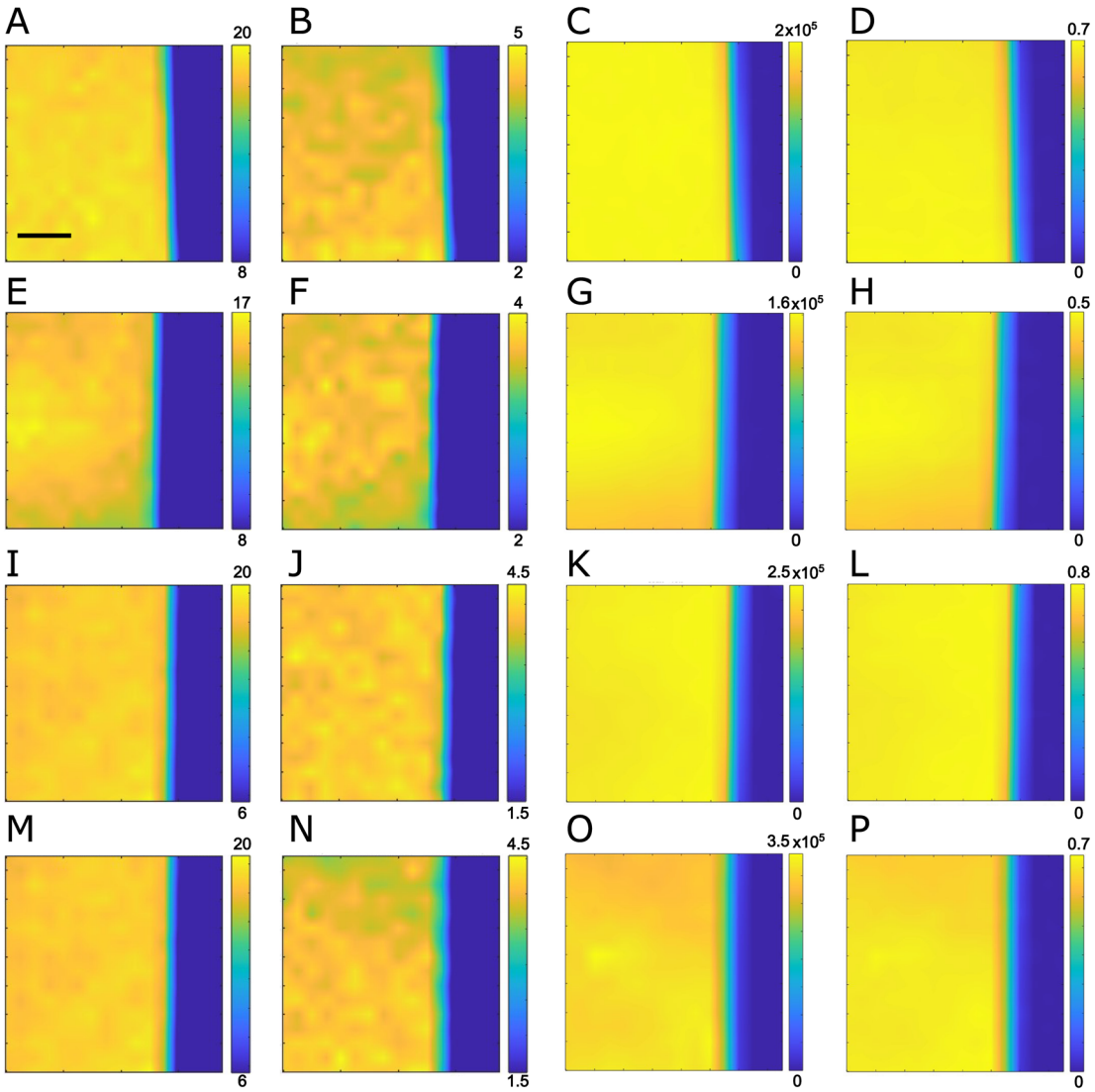


Fig. 7 2D spatial distribution of the X-ray intensity. From the left: $I_{WAXS}/T$ in the amorphous $q$-range, $I_{WAXS}/T$ in the main peak $q$-range, $I_{SAXS}/T$ in the full $q$-range, and $n$. For all maps the background signal (blue area) has been subtracted. (A–D) Control, (E–H) Control 0.1T20, (I–L) 0.2$TiO_2$0.1T20, (M–P) 0.2 NT. Scale bar 1 mm length.

a more dispersed distribution of the data (range = 33 190). This suggests that Tween 20 modified the structure of the protein matrix, and that the strength of the interactions depended on the concentration. These findings also indicate that some of the structural elements of the matrix produce SAXS signals, and hence are hundreds of nanometers in size.

The addition of $TiO_2$ nanoparticles in the form of spheres reduced the $I_{SAXS}/I_T$ value and increased the dispersion of the data compared to the control. Furthermore, in the distribution corresponding to the film reinforced with 0.2% $TiO_2$ nanospheres, another peak appears between 191 000 and 196 000, representing 25% of the data. When these samples were prepared with Tween 20, the dispersion of the data decreased, suggesting that Tween 20 mitigated the disruptive effect of the nanospheres on the protein matrix.

The behaviour of the NT-reinforced films demonstrated significant differences compared to the nanosphere-reinforced films. There was an increase in scattered intensity, particularly noticeable in the film containing the highest concentration of NTs. Additionally, in the sample with 0.1% NTs, the presence of two populations can be observed, with the dominant one (~60%) exhibiting values close to those found for the control with Tween 20 (242 500–255 000). This suggests that the primary effect on the homogeneity of the structure was attributed to Tween 20, while the concentration of NTs remained too low to produce significant structural changes.

In contrast, for the film containing 0.2% NTs, the $I_{SAXS}/I_T$ histogram shifted to higher values. Although two populations were still observed, they were less distinctly defined. This suggests that the presence of NTs at this concentration modified the structure more significantly, consistent with the SEM results indicating that the nanotubes were located within the matrix. At a concentration of 0.2%, the interactions with the protein/Tween 20 matrix were stronger, leading to a more homogeneous

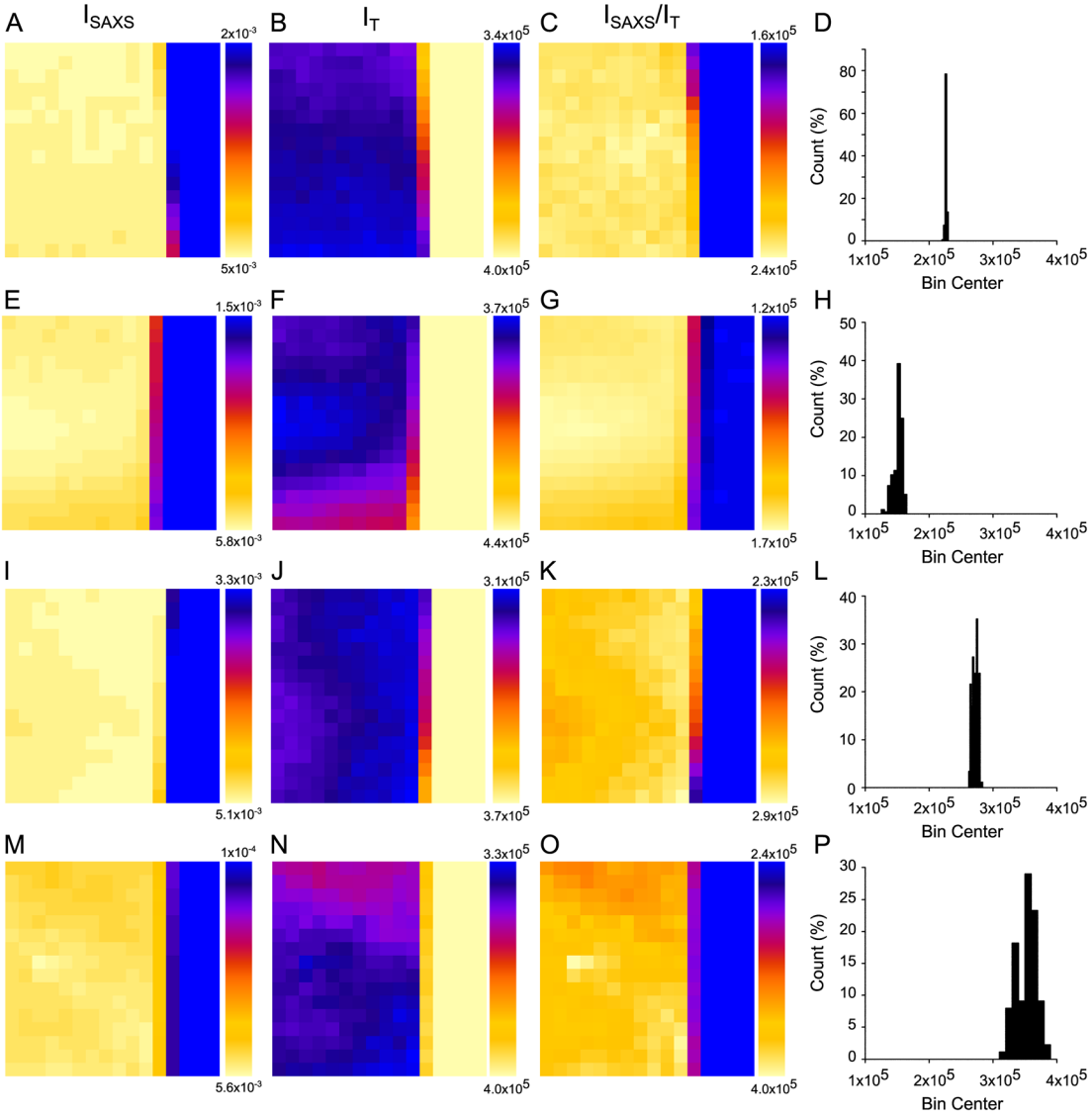


Fig. 8 2D spatial distribution of the X-ray intensity. From the left: scattering ($I_{SAXS}$), transmitted intensity ($I_T$), normalized $I_{SAXS}/T$ maps, and histogram of $I_{SAXS}/T$ values. The right side of each map (blue region in the $I_{SAXS}$ image) corresponds to measures in the no sample region. (A–D) Control, (E–H) control 0.1T20, (I–L) 0.2$TiO_2$0.1T20, (M–P) 0.2 NT. Scale bar 1 mm length.

structure, as evidenced by increased dispersed intensity across all evaluated areas and greater continuity in the values.

The SAXS/WAXS/absorption microscopy results highlighted the importance of the film composition, particularly the Tween 20 content and the morphology of the nanoreinforcement, which was distributed differently in the protein matrix depending on whether the reinforcements were spheres or NTs. The nanoreinforcements varied significantly in size and interacted with the matrix in distinct ways, enhancing or worsening its physical properties based on the nature of the interactions (positive or negative) between the components.

## Conclusions

Whey protein concentrate, omega-3 rich oil, and $TiO_2$ nanocomposite films were successfully prepared. The structure of the films was characterised using advanced techniques, and the distribution of the nanoreinforcements and their effects on the film structure were analysed. This is of great significance, as the film's structure strongly influenced its physical properties. These properties were modified by the formulation, as well as the geometry and concentration of the nanoreinforcements. Tween 20 interacted strongly with the protein, reducing the droplet size of the discontinuous phase in the initial systems, and demonstrating cooperative interactions with the nanoreinforcements in the films. The geometry of the reinforcement played a crucial role in the mechanical and tensile properties. Nanotubes were incorporated within the bulk of the matrix, proving to be more effective in enhancing the storage modulus ($E'$), loss modulus ($E''$), and Young's modulus ($E$) than the nanospheres. In contrast, the nanospheres were primarily located on the surface of the film, resulting in a more heterogeneous structure that better blocked light. The films containing 0.2% nanotubes exhibited the best physical properties of all

 

the films studied, making them promising materials for food packaging applications.

## Data availability

The data supporting this article have been included as part of the ESI.†

## Author contributions

Lina María Rodríguez Pineda, investigation. Dritan Siliqi, formal analysis. Virginia Borroni, formal analysis. Lucas Guz, investigation. Francesco Scattarella, data curation, methodology. Cinzia Giannini, conceptualization. Roberto Jorge Candal, conceptualization. Davide Altamura, writing – review & editing, funding acquisition. Maria Lidia Herrera, writing – original draft, funding acquisition.

## Conflicts of interest

There are no conflicts to declare.

## Acknowledgements

This work was funded by the National Research Council of Argentina and the Consiglio Nazionale delle Ricerche of Italy through the collaborative project Res. 2022-2241-APN-Dir#CONICET: Eco-design, synthesis, and characterization of biodegradable nano-reinforced polymeric films for applications in advanced food packaging, within the Bilateral Agreement CNR/CONICET 2023-2024.

## References

1 M. Alizadeh-Sani, A. Khezerlou and A. Ehsani, Fabrication and characterization of the bionanocomposite film based on whey protein biopolymer loaded with $TiO_2$ nanoparticles, cellulose nanofibers and rosemary essential oil, *Ind. Crops Prod.*, 2018, **124**, 300.

2 X. Zhang, Y. Liu, H. Yong, Y. Qin and J. Liu, Development of multifunctional food packaging films based on chitosan, $TiO_2$ nanoparticles and anthocyanin-rich black plum peel extract, *Food Hydrocolloids*, 2019, **94**, 80.

3 M. Alizadeh-Sani, E. Mohammadian and D. J. McClements, Eco-friendly active packaging consisting of nanostructured biopolymer matrix reinforced with $TiO_2$ and essential oil: Application for preservation of refrigerated meat, *Food Chem.*, 2020, **322**, 126782.

4 H. Hosseini, E. Y. Hamgini, S. M. Jafari and S. Bolourian, Improving the oxidative stability of sunflower seed kernels by edible biopolymeric coatings loaded with rosemary extract, *J. Stored Prod. Res.*, 2020, **89**, 101729.

5 V. G. Kontogianni, E. Kasapidou, P. Mitlianga, M. Mataragas, E. Pappa, E. Kondyli and L. Bosnea, Production, characteristics and application of whey protein films activated with rosemary and sage extract in preserving soft cheese, *LWT – Food Sci. Technol.*, 2022, **155**, 112996.

6 V. Nemati, F. Hashempour-Baltork, M. S. Gharavi-Nakhjavani, E. Feizollahi, L. Marangoni Jr and A. M. Alizadeh, Application of a whey protein edible film incorporated with cumin essential oil in cheese preservation, *Coatings*, 2023, **13**, 1470.

7 G. Ghoshal, Shivani, Thyme essential oil nano-emulsion/tamarind starch/whey protein concentrate novel edible films for tomato packaging, *Food Control*, 2022, **138**, 108990.

8 A. Papadaki, I. K. Lappa, A. C. Manikas, M. G. Pastore Carbone, A. Natsia, V. Kachrimanidou and N. Kopsahelis, Grafting bacterial cellulose nanowhiskers into whey protein/essential oil film composites: Effect on structure, essential oil release and antibacterial properties of films, *Food Hydrocolloids*, 2024, **147**, 109374.

9 Y. Wang, J. Zhang, W. Li, X. Xie, W. Yu, L. Xie, Z. Wei, R. Guo, H. Yan and Q. Zheng, Antibacterial poly(butylene succinate-co-terephthalate)/titanium dioxide/copper oxide nanocomposites films for food packaging applications, *Food Packag. Shelf Life*, 2022, **34**, 101004.

10 W. Zhang and J. W. Rhim, Titanium dioxide ($TiO_2$) for the manufacture of multifunctional active food packaging films, *Food Packag. Shelf Life*, 2022, **31**, 100806.

11 M. Alizadeh Sani, M. Maleki, H. Eghbaljoo-Gharehgheshlaghi, A. Khezerlou, E. Mohammadian, Q. Liu and S. M. Jafari, Titanium dioxide nanoparticles as multifunctional surface-active materials for smart/active nanocomposite packaging films, *Adv. Colloid Interface Sci.*, 2022, **300**, 102593.

12 D. Enescu, A. Dehelean, C. Gonçalves, M. A. Cerqueira, D. A. Magdas, P. Fucinos and L. M. Pastrana, Evaluation of the specific migration according to EU standards of titanium from Chitosan/Metal complexes films containing $TiO_2$ particles into different food simulants. A comparative study of the nano-sized *vs.* micro-sized particles, *Food Packag. Shelf Life*, 2020, **26**, 100579.

13 D. Phothisarattana and N. Harnkarnsujarit, Migration, aggregations and thermal degradation behaviors of $TiO_2$ and ZnO incorporated PBAT/TPS nanocomposite blown films, *Food Packag. Shelf Life*, 2022, **33**, 100901.

14 Z. Feng, L. Li, Q. Wang, G. Wu, C. Liu, B. Jiang and J. Xu, Effect of antioxidant and antimicrobial coating based on whey protein nanofibrils with $TiO_2$ nanotubes on the quality and shelf life of chilled meat, *Int. J. Mol. Sci.*, 2019, **20**, 1184.

15 N. T. Hoyos Merlano, L. Guz, V. Borroni, R. J. Candal and M. L. Herrera, Effects of the geometry of reinforcement on physical properties of sodium caseinate/$TiO_2$ nanocomposite films for applications in food packaging, *Biopolymers*, 2023, **114**, e23531.

16 H. Sayahi, K. Aghapoor, F. Mohsenzadeh, M. M. Morad and H. R. Darabi, $TiO_2$ nanorods integrated with titania nanoparticles: Large specific surface area 1D nanostructures for improved efficiency of dye-sensitized solar cells (DSSCs), *Sol. Energy*, 2021, **215**, 311.

17 P. Samriti, M. C. Joshi, R. K. Gupta and J. Prakash, Hydrothermal synthesis and Ta doping of $TiO_2$ nanorods: Effect of soaking time and doping on optical and charge

transfer properties for enhanced SERS activity, *Mater. Chem. Phys.*, 2022, **278**, 125642.
18 W. S. Rasband, *ImageJ*, U.S. National Institutes of Health, Bethesda, Maryland, USA, 1997, http://imagej.nih.gov/ij/, (Accessed February 2022).
19 H. Yu, Y. Ge, H. Ding, Y. Yan and L. Wang, Vanillin cross-linked chitosan/gelatin bio- polymer film with antioxidant, water resistance and ultraviolet-proof properties, *Int. J. Biol. Macromol.*, 2023, **253**, 126726.
20 S. Estevez-Areco, L. Guz, L. Famá, R. J. Candal and S. Goyanes, Bioactive starch nanocomposite films with antioxidant activity and enhanced mechanical properties obtained by extrusion followed by thermocompression, *Food Hydrocolloids*, 2019, **96**, 518.
21 D. Siliqi, L. De Caro, M. Ladisa, F. Scattarella, A. Mazzone, D. Altamura, T. Sibillano and C. Giannini, Sunbim: A package for x-ray imaging of nano- and biomaterials using saxs, waxs, gisaxs and giwaxs techniques, *J. Appl. Crystallogr.*, 2016, **49**, 1107.
22 F. Scattarella, E. Altamura, P. Albanese, D. Siliqi, M. Ladisa, F. Mavelli, C. Giannini and D. Altamura, Table-top combined scanning X-ray small angle scattering and transmission microscopies of lipid vesicles dispersed in free-standing gel, *RSC Adv.*, 2021, **11**, 484.
23 M. Alizadeh-Sani, J. W. Rhim, M. Azizi-Lalabadi, M. Hemmati-Dinarvand and A. Ehsani, Preparation and characterization of functional sodium caseinate/guar gum/$TiO_2$/cumin essential oil composite film, *Int. J. Biol. Macromol.*, 2020, **145**, 835.
24 M. B. Osuna, A. Michaluk, A. M. Romero, M. A. Judis and N. C. Bertola, Plasticizing effect of Apis mellifera honey on whey protein isolate films, *Biopolymers*, 2022, **113**, e23519.
25 J. Hu, D. Li, Q. Huai, M. Geng, Z. Sun, M. Wang, S. Wang, Y. Li and H. Zheng, Development and evaluation of soybean protein isolate–based antibacterial nanocomposite films containing nano-$TiO_2$, *Ind. Crops Prod.*, 2023, **197**, 116620.
26 M. P. Arrieta, M. A. Peltzer, M. C. Garrigós and A. Jiménez, Structure and mechanical properties of sodium and calcium caseinate edible active films with carvacrol, *J. Food Eng.*, 2013, **114**, 486.
27 M. Jahromi, M. Niakousari, M. T. Golmakani and M. A. Mohammadifar, Physicochemical and structural characterization of sodium caseinate based film-forming solutions and edible films as affected by high methoxyl pectin, *Int. J. Biol. Macromol.*, 2020, **165**, 1949.
28 R. Quevedo, L. G. Carlos, J. M. Aguilera and L. Cadoche, Description of food surfaces and microstructural changes using fractal image texture analysis, *J. Food Eng.*, 2002, **53**, 361.
29 J. Rahimi and M. O. Ngadi, Structure and irregularities of surface of fried batters studied by fractal dimension and lacunarity analysis, *Food Struct.*, 2016, **9**, 13.
30 I. Arzate-Vázquez, J. J. Chanona-Pérez, G. Calderón-Domínguez, E. Terres-Rojas, V. Garibay-Febles, A. Martínez-Rivas and G. F. Gutiérrez-López, Microstructural characterization of chitosan and alginate films by microscopy techniques and texture image análisis, *Carbohydr. Polym.*, 2012, **87**, 289.
31 A. Altomare, C. Cuocci, C. Giacovazzo, A. Moliterni, R. Rizzi, N. Corriero and A. Falcicchio, EXPO2013: a kit of tools for phasing crystal structures from powder data, *J. Appl. Crystallogr.*, 2013, **46**, 1231–1235.